Remote Sensing of Environment 197 (2017) 58–71

Contents lists available at ScienceDirect

Remote Sensing of Environment

journal homepage: www.elsevier.com/locate/rse

Towards wide-swath high-resolution mapping of total ocean surface current vectors from space: Airborne proof-of-concept and validation

Adrien C.H. Martin*, Christine Gommenginger

Marine Physics and Ocean Climate division, National Oceanography Centre, Southampton SO14 3ZH, UK

ARTICLE INFO

Article history:
Received 20 September 2016
Received in revised form 14 April 2017
Accepted 19 May 2017
Available online 29 May 2017

Keywords:
Ocean surface current
SAR
Doppler
Along-track interferometry
Airborne
Validation
Coastal
Bathymetry

ABSTRACT

Two-dimensional high-resolution maps of total surface current vectors obtained for the first time with an airborne demonstrator of the innovative Wavemill instrument concept are validated against HF radar data and compared with output from the POLCOMS high-resolution coastal ocean circulation model. Wavemill is a squinted along-track interferometric SAR system optimized for ocean surface current vector retrieval that operates at moderate incidence angles (~30°) and is compatible with spaceborne implementation. This paper represents the first comprehensive validation of the current retrieval capabilities of squinted along-track SAR interferometry in support of its development as a future European Space Agency Earth Explorer mission.

Wavemill airborne data were acquired in October 2011 in Liverpool Bay off the west coast of Great Britain in light southerly wind (5.5 m/s) and maximum tidal ebbing flow (0.7 m/s) conditions. Contributions to the measured SAR interferometric phase by surface gravity waves, known as the Wind-wave induced Artefact Surface Velocity (WASV), were removed using our best estimate of wind conditions and the (Mouche et al., 2012) empirical correction derived from Envisat ASAR. Validation of the 1.5 km resolution Wavemill current vectors against independent current measurements from HF radar gives very encouraging results, with Wavemill biases and precisions typically better than 0.05 m/s and 0.1 m/s for surface current speed, and better than 10° and 7° for current direction.

The sensitivity of the current retrieval to the wind vector used to compute the WASV is estimated. A ± 1 m/s error (bias) in wind speed has minimal impact on the quality of the retrieved currents. In contrast, the choice of wind direction is critical: a bias of ±15° in the direction of the wind vector degrades the accuracy of the airborne current speed against the HF radar by about ± 0.2 m/s. This highlights the need for future instruments to provide calibrated SAR Normalised Radar Cross Section data to support retrieval of wind and current vectors simultaneously.

Comparisons of POLCOMS surface currents with HF radar data indicate that the model reproduces well the overall temporal evolution of the tidal current (correlation of spatial fields against HF radar over two tidal cycles of 0.9) but that the model features a systematic 1-h delay in the timing of the maximum ebbing flow in eastern parts of the domain near the Mersey Bar Light buoy. At the maximum ebb flow, the model underestimates the current speed (bias of −0.2m/s) with respect to the HF radar and Wavemill data at the time of the flights. Both the HF radar and Wavemill data reflect much greater snapshot spatial variability of the ocean surface current field than is present in the model, resulting in poor correlation of instantaneous spatial fields (< 0.5) between POLCOMS and the HF radar data. The Wavemill data reveal high spatial variability of ocean surface currents at fine scales, which are not visible in the 4km resolution HF radar data. Wavemill detects several strong (1–1.5m/s) localized current jets associated with deeper bathymetry channels in shallow waters (< 10 m) that are too narrow or too close to land to be observed by the HF radar. The study confirms the value of synoptic wide-swath maps of high-resolution ocean surface current vectors for coastal applications and to validate and develop high-resolution ocean circulation models.

1. Introduction

High-resolution satellite images of sea surface temperature and ocean color reveal a multitude of small scale oceanic features that dominate the ocean variability at mesoscales O(10–100)km and

* Corresponding author.
E-mail address: admartin@noc.ac.uk (A. Martin).

http://dx.doi.org/10.1016/j.rse.2017.05.020
0034-4257/

sub-mesoscales O(1–10)km. Submesoscales contain much of the ocean turbulent energy and play a major role in horizontal and vertical mixing, large-scale oceanic transports and ocean biology e.g. Martin and Richards (2001); Lapeyre and Klein (2006b); Lévy et al. (2010); Sasaki et al. (2014). Improved observations and characterization of the ocean variability at the submesoscale are needed to validate ocean circulation models and to develop improved model parameterizations that represent the impact of small oceanic features on the global ocean circulation, air-sea interactions, marine ecosystem responses and long-term climate change.

At present, there are no direct measurements from satellites of total ocean surface current vectors at high resolution. Techniques have been developed to estimate high-resolution current fields by tracking features in series of SST images, using either heat conservation principles or a quasi-geostrophy approach e.g. Emery et al. (1986); Kelly (1989); Lapeyre and Klein (2006a) but the methods have limited applications in cloud-covered regions. Satellite nadir altimeters give all-weather estimates of the across-track component of geostrophic currents but conventional altimeters do not resolve ocean variability in the sea surface height below 70–100 km scales (Dibarboure et al., 2014; Poje et al., 2014). Observing the ocean variability at smaller scales is the prime motivation of the Surface Water and Ocean Topography mission (SWOT), which aims to deliver two-dimensional maps of sea surface height at 1 km resolution using across-track interferometry (XTI) (Fu et al., 2010). From this, SWOT will seek to derive two-dimensional maps of geostrophic current vectors at a resolution of order 10 km over two 70 km swaths. However, there are many ocean surface currents beyond those caused by geostrophy. Other ocean currents that contribute to the total ocean surface current include tides, wind-driven currents, Stokes drift induced by ocean surface waves, currents linked to internal waves and small scale circulation close to unstable stratification. These occur on a multitude of different spatial and temporal scales and are particularly dominant near fronts, at continental shelf breaks and in shallow water and coastal regions.

Microwave imaging radars can remotely provide some direct estimates of the total ocean surface current by measuring the small Doppler shift induced by the ocean surface motion in reflected microwave signals. This has been demonstrated successfully with Synthetic Aperture Radar (SAR) systems using the Doppler Centroid Anomaly method (Shuchman and Meadows, 1980; Rufenach et al., 1983; Chapron et al., 2005) as well as with Along-Track Interferometry (ATI) systems (Goldstein and Zebker, 1987; Goldstein et al., 1989; Romeiser et al., 2014). These systems only measure Doppler signals in one line-of-sight direction, from which the component of the current perpendicular to the satellite track can be determined. Lyzenga et al. (1982) were first to suggest ways of measuring the Doppler signals with one system in several directions, either by using data from two quasi-simultaneous orthogonal flights or by using systems with antennas pointing in two different azimuth directions. A few studies have used orthogonal flights (Shemer et al., 1993; Graber et al., 1996) to derive current vectors but, so far, only the Dual Beam along-track Interferometer (DBI) developed and deployed by the University of Massachusetts (Frasier and Camps, 2001; Farquharson et al., 2004; Toporkov et al., 2005 and the Frequency-Modulated Continuous Wave (FMCW) ATI SAR deployed by the University of Washington (Farquharson et al., 2014a, 2016), have successfully measured current vectors in a single aircraft pass. Both systems use a squint angle of 20° (Toporkov et al., 2005) or 30° (Farquharson et al., 2014b) and very high incidence angles at the boresight (≈60°) to ensure high sensitivity to the surface current. Although these instruments give very good current vector maps, the range of high incidence angles of this concept makes it difficult to implement as a satellite mission (due to instrument power considerations).

Around the same time, a new satellite mission concept called Wavemill was proposed (Buck, 2005) to map both sea surface height and ocean surface fields over two wide swaths with a single system. The original Wavemill concept was conceived as a hybrid interferometer (i.e. including both along-track and across-track interferometric baselines) but the concept gradually evolved to focus on squinted along-track interferometry in order to optimize the retrieval of ocean current vectors. Wavemill differs from the DBI in two main respects: through the use of larger squint angles (∼45°) and of relatively low incidence angles (∼30°) that make it compatible with spaceborne implementation.

An airborne demonstrator of the Wavemill concept was developed and flown by Airbus Defence and Space UK in the frame of a European Space Agency project. Airborne data were acquired during the Wavemill proof-of-concept experiment, which took place in October 2011 in Liverpool Bay off the west coast of Great Britain. This paper presents the first comprehensive analysis of the surface current retrieval capabilities of the Wavemill concept during the campaign, including validation against independent in situ current measurements from HF radar and comparison with output from a high-resolution ocean circulation model. A small subset of these data acquired in a 7× 7 km^2 box around the Mersey Bar Light buoy (Fig. 1) were previously examined in Martin et al. (2016) to estimate the impact of ocean surface waves on Wavemill currents through the Wind-wave Artifact Surface Velocity (WASV). However, the analyses in this paper are not based on the WASV correction derived in Martin et al. (2016), and therefore constitute an entirely new and independent assessment of the capabilities of squinted SAR interferometry in support of its development as a spaceborne mission.

The paper is arranged as follows. Section 2 presents the Wavemill airborne campaign, the Wavemill airborne system and measurements, and the ancillary in situ and model data used in the analyses. The method to retrieve surface current vectors from the Wavemill airborne measurements and to correct for the WASV is presented in Section 3. Results are presented in Section 4 and discussed in Section 5. The paper closes with conclusions in Section 6.

2. Datasets

2.1. Overview of Wavemill airborne campaign

The Wavemill Proof-of-Concept Campaign was carried out in the last week of October 2011 over various sites in the Irish Sea off the

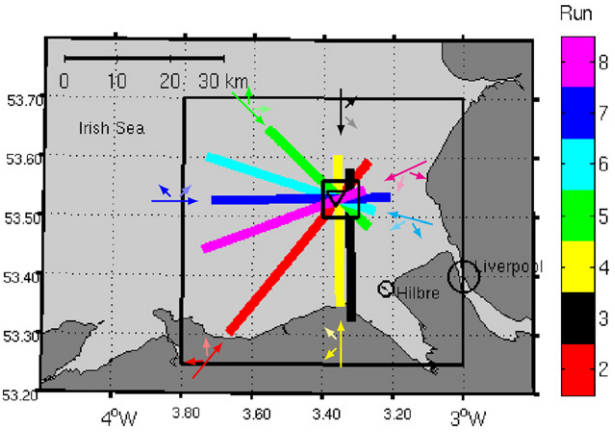

Fig. 1. Location of Wavemill airborne proof-of-concept data in the Liverpool Bay off the west coast of Great Britain, UK. Each run is represented by a different color. For each run, the long colored arrow represents the aircraft flight direction and the two small arrows represent the line-of-sight directions of the fore (pale color) and aft (bright color) pairs of antennas. The positions of Liverpool city and Hilbre Island are indicated by black circles. The triangle represents the position of the Mersey Bar Light (MBL) buoy. The small square around MBL represents the 7×7 km^2 area used in Martin et al. (2016) and for inter-run bias correction in this study. The larger square represents the study area presented in Figs. 4 and 5.

Table 1
Retrieval performance of the Wavemill airborne current vectors (1.5km resolution) versus HF radar (4km resolution averaged over the 80min flight duration).

Run ID number	Median flight time (UTC)	Number of samples	Current speed (m/s)			Current direction (°)		
			Bias	std	RMSE	Bias	std	RMSE
2	00h18	27	0.06	0.19	0.20	−11	9	14
3	00h31	N/A	N/A	N/A	N/A	N/A	N/A	N/A
4	00h40	9	−0.05	0.06	0.07	−11	7	13
5	00h53	15	−0.04	0.14	0.14	−5	6	8
6	01h04	20	−0.01	0.10	0.09	−9	5	10
7	01h16	21	0.05	0.05	0.07	−3	7	7
8	01h27	20	0.13	0.11	0.17	−10	4	11
all		112	0.04	0.14	0.14	−8	7	11

west coast of Great Britain (United Kingdom). The proof-of-concept campaign and geophysical conditions were previously characterized in Martin et al. (2016) but are briefly recalled here for convenience.

Two scientific flights took place over two days, but only data acquired on 26 October 2011 are presented in this paper. The bulk of the airborne data acquired that day consisted of a large star pattern spanning almost 40 km (see Fig. 1). Martin et al. (2016) analyzed a small data subset acquired over a 7×7 km^2 box centered over the Mersey Bar Light (MBL) buoy to characterize the Wind-wave Artefact Surface Velocity (WASV) against ADCP measurements. The analyses in this paper concern all the data acquired in the "star pattern" over the Liverpool Bay, thus covering a wider range of conditions and providing a wider assessment of the retrieved Wavemill surface current vectors against the HF radar data.

The data considered in this paper are represented in Fig. 1, showing the full "star pattern" of seven runs in seven different heading directions, centered over the Mersey Bar Light (MBL) buoy where in situ current and wave measurements were available. Throughout the paper, each run is identified by a number (R2, R3, etc.) and a given color shown in the color bar in Fig. 1. For each run, the long arrows represent the flight direction of the aircraft and the two small arrows represent the line of sight of the fore- and aft-looking pairs of antennas (in pale and bright colors respectively). Note that, for run R3 (black), only data acquired for the fore-looking antenna pair were available for the full run.

All airborne data in the star pattern were acquired within 80 min of each other between 00:13UTC and 01:31UTC during the maximum ebbing tidal flow (∼0.7 m/s westward). The median acquisition time of each run is indicated in Table 1. The geophysical conditions during the flights, as previously characterized in Martin et al. (2016), consist of a steady ebbing tidal current (westward current) of about 0.7 m/s, a wind of about 5.5 m/s from the South (direction ∼200°) and a weak swell system ($H_s = 0.5$ m, $\lambda = 53$ m) traveling into the area from the North-West.

2.2. Wavemill airborne system

The Wavemill airborne demonstrator was developed and deployed by Airbus Defence and Space UK in the frame of a European Space Agency project. Only the main characteristics of the system are given here and summarized in Table 2, as further information is available in Martin et al. (2016) and Wavemill PoC Team (2012).

The system operates at X-band (9.55 GHz) with a 100 MHz bandwidth and both transmit and receive using vertical polarization (VV). The interferometric system is composed of two pairs of antennas, looking in pairs ±45° fore and aft of the aircraft broadside and mounted on a gimbal, which mitigated aircraft attitude changes in roll and pitch. Each pair of antennas is composed of one emit/receive antenna and one receive-only antenna. The physical baseline for each pair is 50 cm. Given an average aircraft velocity (V_p) around 80 m/s, the time lag (τ) between the two receiving antenna phase centers is about 3 ms.

The antenna beamwidth is 30° in elevation. Data acquisition was performed over incidence angles ranging from 24° (near range) to 45° (far range). The swath width was about 1800 m. The SAR focusing was performed over lines of constant Doppler frequencies, which implies that the squint angle on the ground varies across the swath (e.g. ±65° at 24° of incidence angle and ±32° at 45° of incidence angle).

The interferogram is a pixel-to-pixel phase difference between the two complex SAR images defined as $\Delta\phi_j = \arg\left(M_j.S_j^*\right)$ with $j = 1, 2$ and where M and S refer to the single look complex (SLC) images of the master (M) or the slave (S) antenna of each antenna pair. The subscripts $j = 1, 2$ represent respectively the fore- and aft-looking antenna pairs. Absolute calibration was applied to the interferometric phase as described in Wavemill PoC Team (2012) and Martin et al. (2016), but no provision was made to calibrate the amplitude of the SAR images. This lead to unknown differences between images from the fore- and aft-looking antennas and prevented the estimation of surface wind vectors directly from the Wavemill airborne data.

2.3. Ancillary datasets

A wide range of ancillary datasets were available in the flight campaign area, both from in situ observations and high-resolution numerical models to support the assessment of the Wavemill data.

A WERA HF radar system provided measurements of surface current vectors in the Liverpool Bay every 20 min. The HF radar ground-based antennas were located at Formby Point and in Llanddulas, indicated as black stars in Fig. 2-a. The HF radar operates at 12–16 MHz that corresponds to a Bragg wavelength of 12–9 m. The system reports surface current vectors every 20 min, averaged over 9 min and cells of 4×4km^2. Typical radial current velocity error for this type of system is estimated around ∼0.05 m/s (Liu et al., 2014). The errors on the current vector magnitude and direction vary across the HF radar domain as they depend on the location of each cell relative to the line-of-sights of the two HF radar antennas.

Table 2
Main characteristics of the Wavemill airborne demonstrator.

Center frequency	9.55 GHz
Pulse bandwidth	100 MHz
SAR processed bandwidth	75 Hz
Polarization	VV
Physical baseline between antenna pairs	50 cm
Squint angle (mid swath)	±45°
Elevation beamwidth	30°
Azimuth beamwidth	30°
Incidence angle range	24° – 45°
Altitude	2790 m
Aircraft speed	66–87 m/s
Swath width	1800 m
Image spatial resolution in range	5.3 to 1.5 m
Image spatial resolution in azimuth	1.06 m

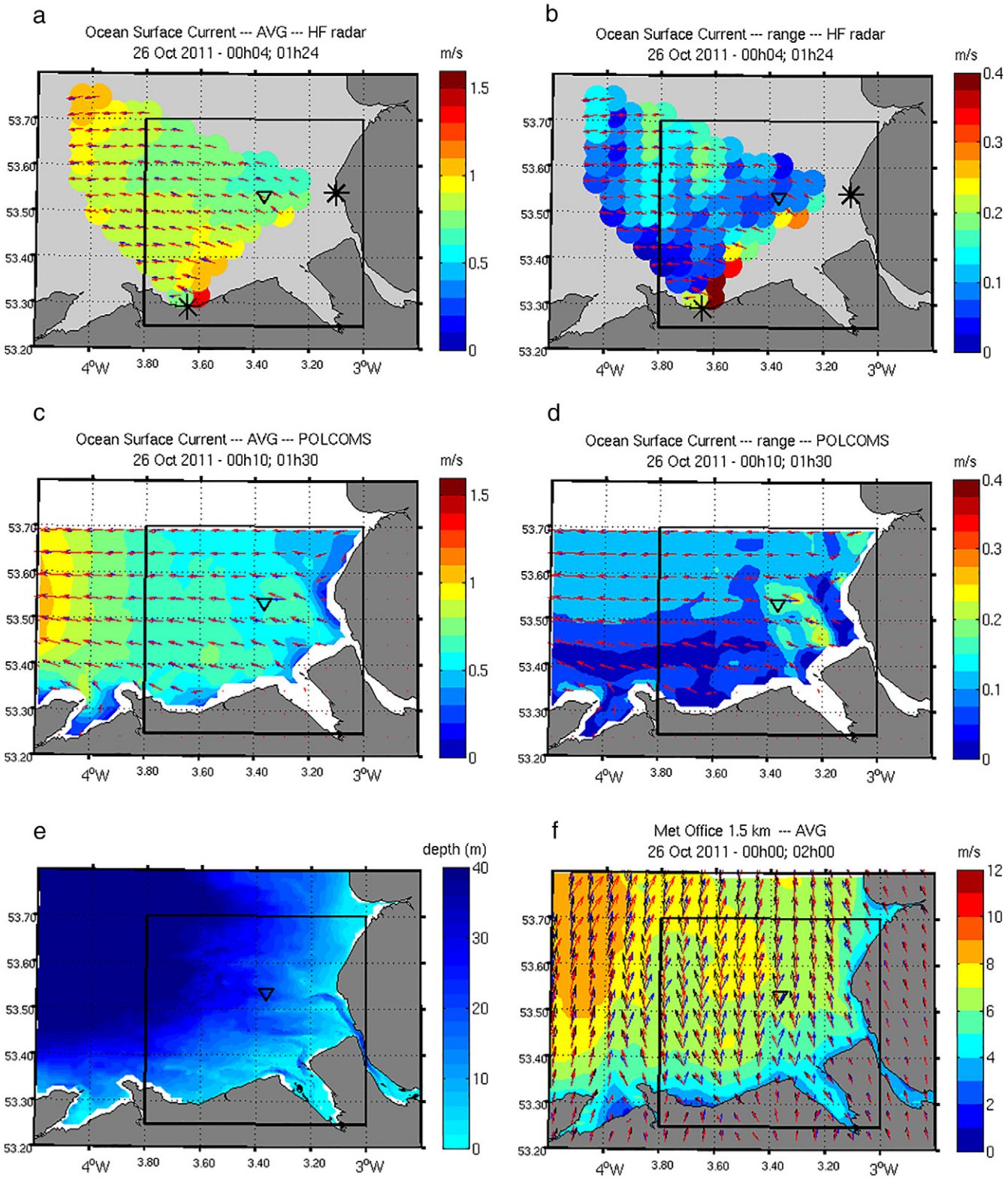

Fig. 2. (a) HF radar current speed (available every 20 min) averaged over the 80 min Wavemill flight period (00h04–01h24). Color circles represent current velocity for each radar cells of 4 km. (b) HF radar current speed range (max-min) over the same period as (a). (c) POLCOMS surface current speed (available every 10 min) averaged over 80 min (00h10–01h30) (d) POLCOMS surface current speed range over the same period as (c). (a to d) blue and red arrows represent the first and last current vector observed over the relevant period. (e) Bathymetry at 180 m resolution over Liverpool Bay (East of 3.7°W) and 1 km resolution over the rest of the Irish Sea. (f) High resolution (1.5 km) winds from the MetOffice UKV atmospheric forecasts. Colored arrows represent wind direction at 00h00 (blue), 01h00 (red) and 02h00 UTC (black). Wind vector grid is subsampled to 4.5 km to improve readability. Wind speed shown in color is the average of the wind at these three times.

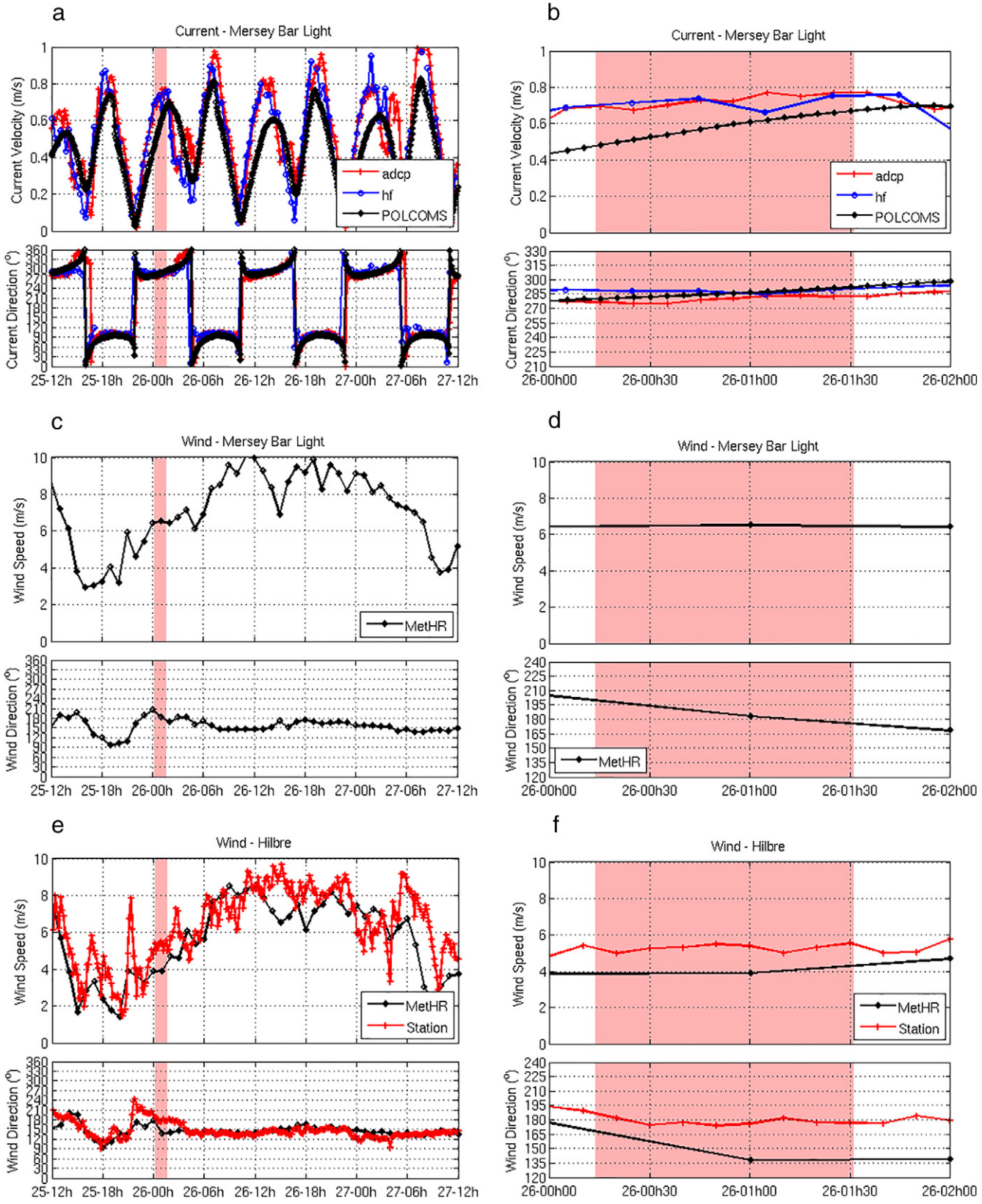

Fig. 3. Time series of (top) current surface at Mersey Bar Light (MBL) from the ADCP, HF radar cell, and POLCOMS outputs; (middle) wind at MBL from the MetOffice high-resolution outputs; (bottom) wind at Hilbre Island from the station and the MetOffice high-resolution outputs. Time series for (left) 48h and (right) 2h. The duration of the star pattern flights is represented with pink color background.

Fig. 2-a shows the HF radar current velocity averaged over the 80 min flight period, while Fig. 2-b shows the range of the HF radar current velocity (defined as the difference between the maximum and minimum value) over the same period. On both figures, the current vectors observed by the HF radar at the beginning and end of the flight period are indicated as blue and red arrows. Outlier values of current and current range for HF radar cells at the coast and along the line-of-sight between the two ground-based HF radar stations suggest slightly lower reliability of the HF radar current data in those cells.

The black triangle in Fig. 2 indicates the position of the Mersey Bar Light (MBL) buoy. In situ observations of ocean currents were available from an upward-looking Acoustic Doppler Current Profiler (ADCP) located near MBL. The ADCP was placed on a sea bed-mounted frame in 23.5 m water close to the MBL. Ocean currents at the surface were estimated from the ADCP by taking measurements from the near-surface vertical bin located approximately 19.7 m above the seabed, which correspond to a position between 4 and 2 m below the sea surface as the tide ebbed during the flight campaign. The ADCP gives measurements every 10 min, with a reported accuracy of ~0.01 m/s. Fig. 3-a and b show the temporal variations of the current magnitude and direction at MBL over 48 h and over the 80 min flight period (pink highlight) measured by the ADCP (red) and the HF radar data (blue).

Ocean surface current output was obtained from the NOC POLCOMS (Proudman Oceanographic Laboratory Coastal Ocean Modelling System) high-resolution ocean circulation model (Holt and James, 2001; Lane, 2008) run in its Irish Sea configuration with a spatial resolution of 1.8 km. Output data are available every 5 min. The fine resolution Irish Sea domain is nested in the coarser resolution Atlantic margin ocean model, which provides boundary conditions. The ocean model is forced using atmospheric forecasts from the Met Office North Atlantic European model at 12 km resolution (Waller et al., 2014). The POLCOMS average surface current and range during the flight campaign are shown in Fig. 2-c and d. Fig. 3-a and b show the temporal variations of the current magnitude and direction at MBL over 48 h and over the flight period estimated by POLCOMS (black), superposed with the HF radar and ADCP data.

High resolution bathymetry was available and is represented on Fig. 2-e. The resolution is 180 m in Liverpool Bay and 1 km in the rest of the Irish Sea (Lane, 2008). Water depth over the area increases smoothly with increasing distance from the coast, except for a few well-delimited deep-water channels seen at the mouths of the river estuaries.

In situ wind and wave measurements were available at two locations across the site, including wind measurements from a coastal weather station at Hilbre Island every 10 min, and directional wave spectra at MBL every 30 min. No wind data were available at MBL. These measurements are unfortunately insufficient to reveal any spatial variability of the wind field across the domain, particularly near the coast. Wind conditions at Hilbre Island over 48 h and over the flight period are shown in Fig. 3-e and d. Overall, based on analyses of wind and wave data at Hilbre and MBL in Martin et al. (2016), the wind conditions are assumed to be uniform across the domain, with a magnitude of 5.5 m/s from the South (200°).

Wind output was also obtained from the Met Office atmospheric forecasts (UKV; (Waller et al., 2014), available hourly on a 1.5 km grid. A map of the wind conditions forecast for the period of the campaign is represented in Fig. 2-f. The model forecast winds indicate considerable spatial variability in wind velocity across the domain, as well as wind direction changes over the period of the campaign. Fig. 3-c to f show the forecast winds over 48 h and over the flight period at MBL and Hilbre Island. While the agreement at Hilbre is encouraging overall, the forecast winds differ noticeably in magnitude and direction from the data at Hilbre during the period of the flight, and are therefore only used to provide qualitative context in the analyses that follow.

3. Deriving surface current vectors from Wavemill airborne data

Microwave radar instruments sense the Doppler shift induced by the displacement of a target in the radar line-of-sight. The Doppler shift can be related directly to the radial velocity of the target in the radar slant range direction. When the sea surface is the target, the radial velocity results from the projection in the slant range direction of the sea surface velocity in the radial direction. The surface radial velocity is the sum of the surface current in the radar line-of-sight direction (related to the effective horizontal water mass transport in that azimuth angle direction) and an unwanted Wind-wave induced Artefact Surface Velocity (WASV) linked to microwave scattering processes (Table 3). The WASV is caused by the phase velocity of the surface scatterers responsible for the microwave backscatter (e.g. Bragg waves), the orbital velocity of ocean surface gravity waves and the radar response to the surface (Chapron et al., 2005). The WASV has been estimated empirically and found to depend on wind speed, relative wind direction and incidence angle (Mouche et al., 2012; Martin et al., 2016). The WASV has to be estimated and removed from the surface radial velocity in order to retrieve the surface current in that direction. By repeating the process in two azimuth directions, one can compute the surface current speed and direction. These steps are described more fully below:

3.1. Step 1: Estimate surface radial velocity in fore and aft direction

The radial velocity of the surface, u_{rsv}, is related to the velocity measured by the radar in the line-of-sight (u_r) projected on the surface, i.e.:

$$u_{rsv} = \frac{u_r}{\sin\theta} \tag{1}$$

It has been shown that this can be related to the interferogram $\Delta\phi_j$ e.g. Graber et al. (1996) using:

$$u^j_{rsv} = -\frac{V_p}{k_e B}\frac{\Delta\phi_j}{\sin\theta} \approx -\frac{0.7\Delta\phi_j}{\sin\theta} \tag{2}$$

with k_e the radar wavenumber, V_p the aircraft velocity, B the physical baseline, θ the incidence angle and the subscript j represents either the fore- or aft-looking antenna pair.

The radial surface velocity measured with the Wavemill fore and aft-looking antenna pairs for all runs is presented in Fig. 4-a and b. Note that these radial surface velocity measurements include both the WASV and the radial surface current in that direction and cannot be compared directly with independent ocean current data. In this paper, the terms “velocity” and “current” are not interchangeable: “velocity” refers to a radar instrument measurement while “current” refers to the geophysical property of the sea surface. Comparison of Wavemill or SAR Doppler Centroid data against independent ocean current estimates cannot proceed until the WASV has been removed.

Table 3
Variable denomination.

u_r	Radial velocity in the line-of-sight
u_{rsv}	Radial surface velocity (projected u_r)
u_{rsc}	Radial surface current ($u_{rsv} - WASV$)

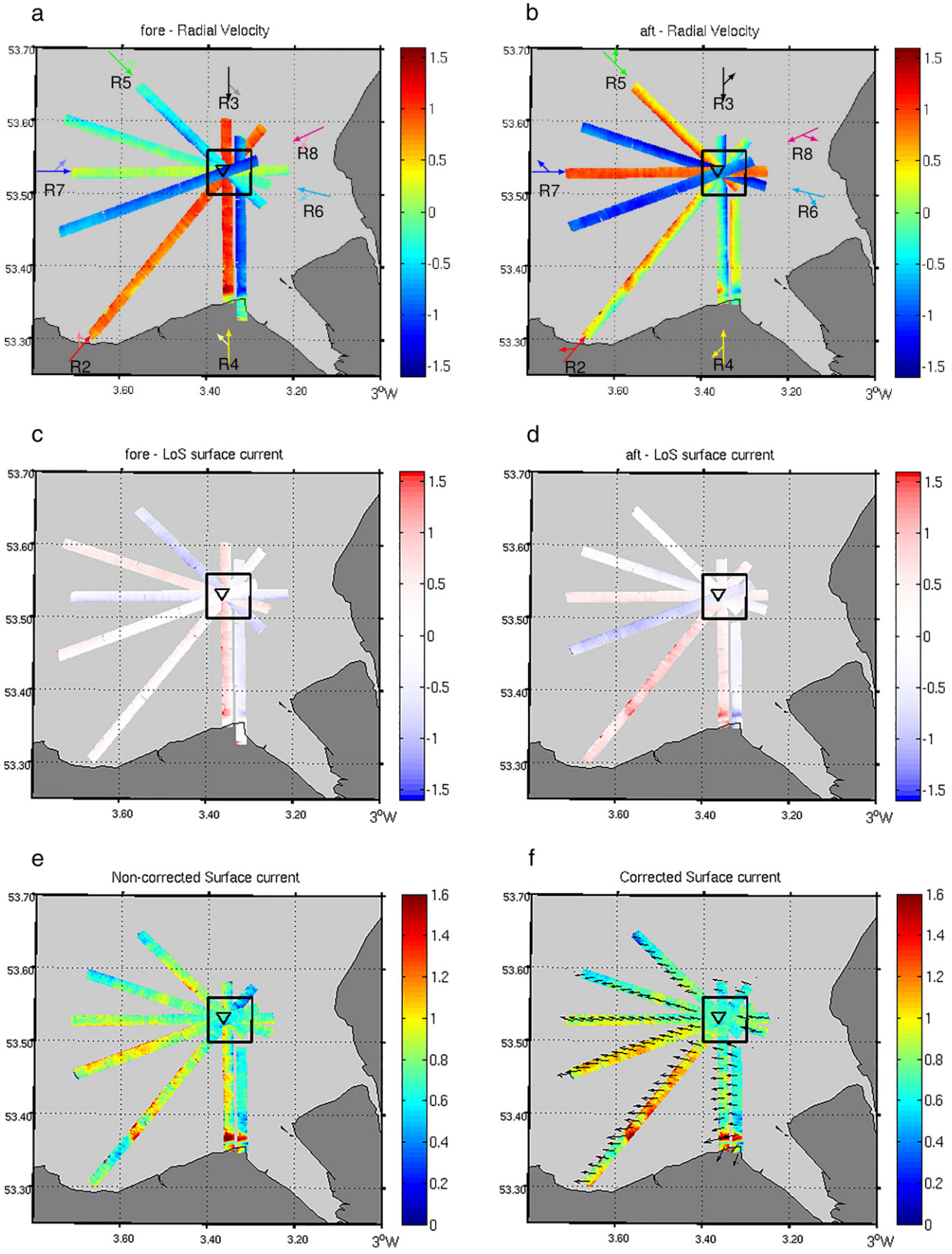

Fig. 4. Wavemill airborne results showing (top) radial surface velocity from the (a) fore- and (b) aft-looking antenna pair; (middle) radial surface current after WASV correction from the (c) fore- and (d) aft-looking antenna pair; (e) retrieved surface current magnitude; (f) surface current magnitude and direction after correction for inter-run biases at MBL. The triangle represents the position of MBL. The square represents the 7× 7 km^2 box centered over MBL used to estimate inter-run biases in surface current. The position of R3 is shifted 0.03° eastward to avoid overlapping with R4 and improve readability.

3.2. Step 2: Correct surface radial velocity for the WASV

In this study, the WASV is removed using the C-DOP model (Mouche et al., 2012). C-DOP is an empirical model developed from Envisat C-band ASAR Doppler Centroid Anomaly estimates collocated with ECMWF winds. The model provides the means to estimate the Doppler shift induced by wind waves in SAR through a simple dependence on the wind vector and incidence angle. Martin et al. (2016) revealed remarkably good agreement between the C-band spaceborne C-DOP model and the Wind-wave Artifact Velocity derived from the X-band airborne Wavemill estimates. The reader should refer to Martin et al. (2016) paper for an extensive discussion of this remarkable agreement.

To first order, the WASV is strongly determined by the wind direction relative to the radar look direction, with maximal amplitude of the WASV observed in the upwind/downwind direction. In comparison, wind speed and incidence angle are second order effects on the magnitude of the WASV.

The radial surface current, u^j_{rsc}, for each antenna pair look direction is obtained by subtracting the WASV estimated with C-DOP from the radial surface velocity, i.e.:

$$u^j_{rsc} = u^j_{rsv} - \mathrm{WASV}(\varphi^j, u_{10}, \theta), \tag{3}$$

with the subscript j representing either the fore- or aft-looking antenna pair, φ^j the wind direction relative to the antenna pair look direction, u_{10} the wind speed and θ the incidence angle. Radial surface currents for the fore and aft-looking antenna pairs are presented respectively in Fig. 4-c and d. Blue (red) colors represent water approaching (resp. receding) from the Wavemill antenna. The colors are consistent with a westward ebbing flow.

The low energetic swell is not noticeable either in the SAR amplitude data or in the Doppler observations (interferometric phase — not shown). In the presence of stronger swell as in e.g. Romeiser et al. (2014), it would have been necessary to remove this contribution before proceeding with estimating the surface current vectors (next section).

3.3. Step 3: Estimate ocean surface current vectors

The magnitude ($|c|$) and direction (Ψ) of the surface current vector are retrieved by combining the radial surface currents in two azimuth directions estimated by the fore and aft-looking antenna pairs, which are looking about 90° from each other. As the effective squint angle across the swath is not constant, it is necessary to take into account the range dependent effective angle at the surface between the fore and aft-looking antennas (ψ_{squint}) for each pixel in the swath, as follows:

$$|c| = \sqrt{\frac{u^{fore^2}_{rsc} + u^{aft^2}_{rsc} - 2 * u^{fore}_{rsc} * u^{aft}_{rsc} * \cos(\psi_{squint})}{\sin(\psi_{squint})^2}}, \tag{4}$$

$$\Psi = azi^{fore} - \arccos\left(\frac{u^{fore}_{rsc}}{|c|}\right) \mathrm{if} u^{aft}_{rsc} > u^{fore}_{rsc} * \cos(\psi_{squint}), \tag{5}$$

$$= azi^{fore} + \arccos\left(\frac{u^{fore}_{rsc}}{|c|}\right) \mathrm{otherwise}, \tag{6}$$

with azi^{fore} the azimuth direction of the fore-looking antennas.

The magnitude of the retrieved surface current is mapped in Fig. 4-e.

3.4. Step 4: Correct for Wavemill airborne inter-run biases at cross-overs

Without further correction, the currents retrieved from different runs display small inter-run biases in the MBL area (7× 7 km^2 box centered over MBL) where the different runs overlap. The inter-run biases are of the order of ±0.1 m/s in north and east current components and vary slowly with incidence angle (not shown). The star pattern crossovers at MBL give the means of empirically estimating and removing these residual inter-run biases. This correction is not intended to provide absolute calibration and this step is obviously specific to this campaign and not generally applicable.

The median value of the retrieved current vector over MBL estimated for all runs (except R3 for which no current data was retrieved over the MBL area) is 0.71 m/s for the current magnitude and 280° for direction (north and east components respectively 0.12 m/s and −0.69 m/s). The retrieved current vectors for each run and at each incidence angle were subsequently adjusted to ensure that the mean current vector over the MBL area in each run matches the all-run median value over the same area.

The surface current vectors obtained after inter-run bias correction are presented in Fig. 4-f. Correcting for the biases results in a spatially more consistent current vector field over the domain, with no inter-run differences over the MBL area. It is these bias-corrected Wavemill current data that are used in the validation and comparisons that follow.

4. Results

4.1. Validation against HF radar and ADCP

The Wavemill airborne surface currents are originally retrieved at a spatial resolution of 100 m (to mitigate the noise in the SAR data) but the current data were subsampled for these analyses to 1.5 km to facilitate validation against HF radar current estimates (at 4 km resolution). The 1.5 km resolution is primarily determined by the 1.8 km maximum swath width of the airborne Wavemill instrument.

Fig. 5-a presents the Wavemill surface current vectors obtained at 1.5 km resolution (small colored circles and red arrows) plotted over the surface currents measured by the HF radar (large colored circles and black arrows) averaged over the duration of the flight. Differences between the Wavemill current and the HF radar current at the locations of the Wavemill data are presented in Fig. 5-b. Overall, the Wavemill currents show similar spatial patterns and magnitudes as those observed by the HF radar, without any systematic biases over the domain.

Table 1 gives the mean bias, standard deviation (std) and root-mean-square error (RMSE) of the Wavemill minus HF radar current differences for all runs and for separate runs. The overall bias against the HF radar is ±0.04 m/s, with biases for individual runs typically equal or below ±0.05 m/s. Only R2 and R8 tend to retrieve stronger currents than the HF radar (except close to the coast for R2), leading to biases of 0.13 m/s for R8 and 0.06 m/s for R2. Except for runs R2, R5 and R8, the runs report precisions (std) versus HF radar better than 0.1 m/s. The overall precision is slightly worse (0.14 m/s), being strongly affected by the larger values obtained for R2 and R8.

Fig. 5-c presents the Wavemill and HF radar current as a scatter plot. It shows relatively good agreement between currents from Wavemill and from the HF radar, while depicting a slightly smaller dynamic range of the HF radar currents compared to Wavemill (Fig. 5-c) that could be linked to the difference in spatial resolution between the Wavemill and HF radar current products.

Over the MBL area, the Wavemill median current (0.71 m/s, 280°) is in very good agreement with the ADCP estimate (0.73 m/s and 279°) and with the current magnitude from the HF radar (0.73

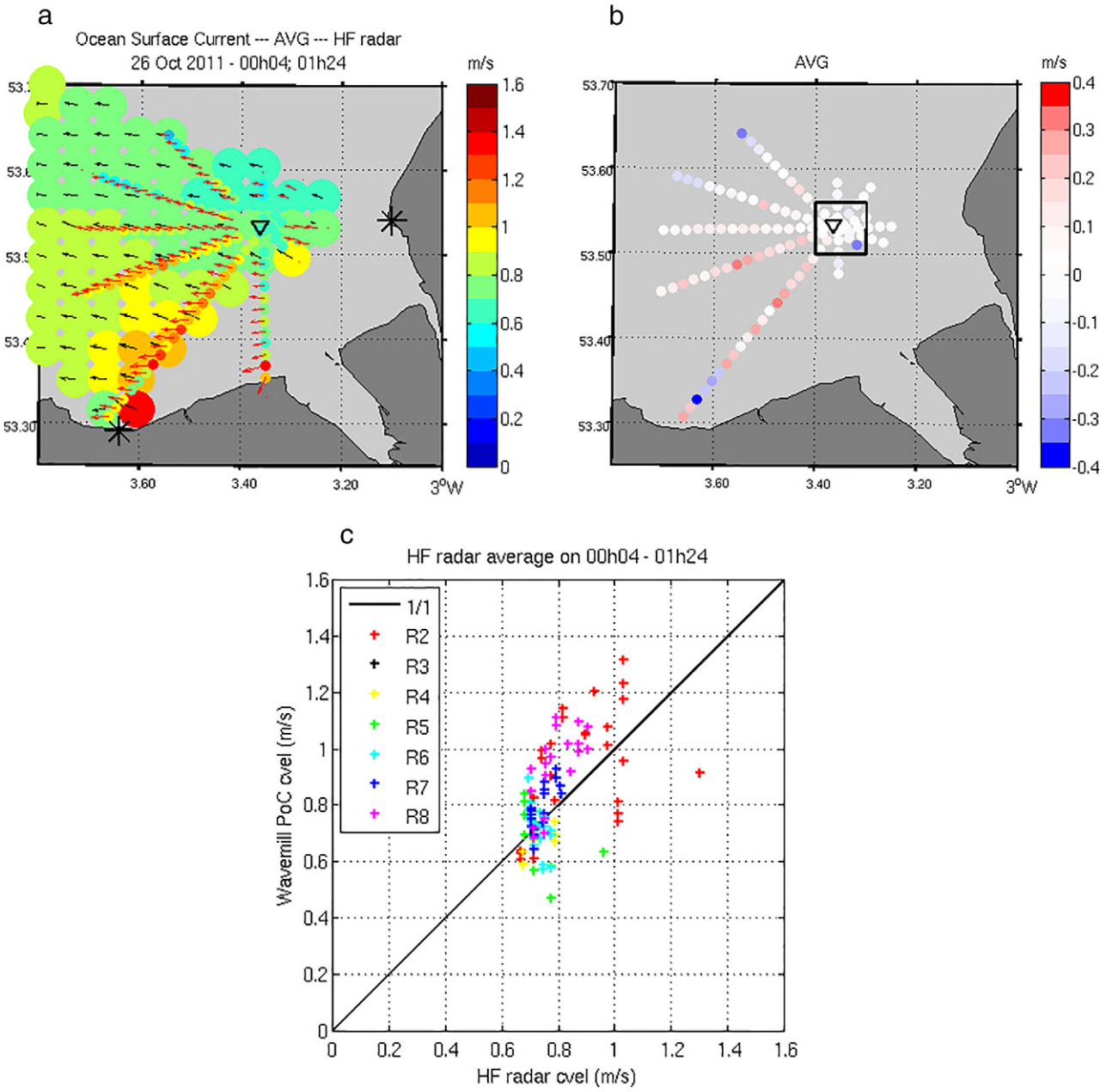

Fig. 5. (a) Surface current speed and direction from Wavemill superposed over HF radar data. Small colored circles and red arrows represent the surface currents from Wavemill at 1.5km resolution. Large colored circles and black arrows represent the surface currents from the HF radar at 4km resolution averaged over the 80min duration of the flights. The two black stars onshore represent the positions of the HF radar antennas. (b) Differences between the Wavemill and HF radar current speed at the locations of the Wavemill data. White circles correspond to 0m/s bias. (c) Scatterplot of the Wavemill surface current at 1.5km resolution against colocated HF radar surface currents averaged over the 80min duration of the flights.

m/s). The HF radar current direction at MBL (288°) differs from both Wavemill and the ADCP by about 9°.

Over the full domain, the Wavemill current direction is slightly biased overall against the HF radar (Fig. 5-a) by about −8° (Table 1), which is consistent with the difference observed between the ADCP and the HF radar at MBL. Thus, the current direction differences between Wavemill and the HF radar could be linked to genuine differences in how Wavemill and HF radar sense sea surface currents.

4.2. Sensitivity of the Wavemill retrieved current to wind vector

As explained in Section 3, the retrieval of surface current requires correcting for the WASV, which is strongly determined by wind, particularly wind direction. In the previous section, the WASV was estimated using a nominal wind vector (5.5 m/s from 200°) assumed constant over the whole area. In this section, we consider the sensitivity of the WASV, and consequently of the retrieved Wavemill currents, on the choice of wind vector used for the WASV correction. The approach is to re-compute the Wavemill retrieved currents (and its statistics) for slightly different wind conditions to determine the impact of wind errors on the retrieved currents.

The Met Office high-resolution atmospheric forecast winds indicate a spatio-temporal variability of the wind vector in this region of the order of 0.6 m/s and 13° (inter-quartile range over the studied area for 3 h around the time of the flights). This is slightly smaller than the precision of ±1 m/s and ±15° reported for MetOp ASCAT

wind vectors against buoys (Bentamy et al., 2016), which are the values we will use here.

An uncertainty on the wind of ±1 m/s and ±15° was added to the nominal wind of 5.5 m/s and 200°. Changing wind speed by 1 m/s up or down has little impact on the retrieved current statistics against HF radar current, where overall biases change by no more than 0.02 m/s and 6° compared to the values in Table 1. The bias in current direction against HF radar actually reduces slightly when the wind speed is lowered by 1 m/s.

In contrast, changing wind direction by ±15° significantly degrades the statistics of the retrieved currents, increasing its biases against HF radar by about ±0.2 m/s. The impact on current direction is weaker however, with biases reaching no more than 4°.

These results highlight the critical need for accurate knowledge of wind direction to achieve accurate surface current retrieval with Wavemill. It reinforces the message about the need for fully calibrated amplitude data from which normalized radar cross section can be estimated in order to estimate wind directly from the Wavemill data at each location. Ultimately, Wavemill will need to retrieve current and wind vectors simultaneously by exploiting its backscatter and Doppler capability and multi-azimuth diversity (together with polarization diversity if necessary).

4.3. Comparison with POLCOMS high-resolution ocean circulation model output

High-resolution ocean circulation models offer one of few means of estimating and predicting ocean currents and their spatio-temporal variability in strategically important ocean regions such as the coastal zone, thereby providing valuable information in support of many economic, ecological and societal needs. Apart from HF radars, there is little other spatially-distributed data available to validate these models. One of the objectives of a future new spaceborne mission would be to provide wide-swath high-resolution maps of current vectors to help validate and improve ocean circulation models, particularly in coastal, shelf- and ice-covered seas.

POLCOMS is a well-established high-resolution ocean circulation model that has seen extensive validation in the Irish Sea. In this section, the POLCOMS data are first compared against the HF radar data to determine to what extent the high-resolution ocean circulation model output can be used to validate Wavemill. The POLCOMS output is then briefly compared with Wavemill to illustrate how Wavemill's synoptic maps of surface current vectors can provide valuable measurements to validate and develop high-resolution models in the absence of HF radar data.

Fig. 2-c shows the map of POLCOMS surface current vectors averaged over the period of the Wavemill flight. Differences between POLCOMS (Fig. 2-c) and HF radar current (Fig. 2-a) at the time of the Wavemill flights immediately highlight the negative bias in the magnitude of the POLCOMS surface currents (−0.19 m/s). Direct comparison of the spatial fields in Fig. 2-c and a result in poor correlation for current magnitude (0.3) and direction (0.5).

Fig. 3-a shows the time series of the POLCOMS, HF radar and ADCP surface currents at MBL over 48 h close to the time of the Wavemill flights. It reveals that, while the model captures the magnitude and temporal variation of the tidal current reasonably well over most of the tidal cycle, there are issues with the timing and the magnitude of the maximum ebbing flow at MBL, which is delayed in the model by about 1 h. At MBL, the shift in the timing of the maximum ebbing flow leads to POLCOMS underestimating the current magnitude by 0.2 m/s at the time of the Wavemill flights. This 1 h delay is observed only in the vicinity of MBL. The model otherwise shows excellent agreement with HF radar and ADCP for the rest of the tidal cycle.

When considering POLCOMS and HF radar data over the full domain and the full 48 h period shown in Fig. 3-a, POLCOMS shows high correlation with the HF radar for both current magnitude (0.93) and direction (0.88). Overall, POLCOMS average current magnitude is biased against the HF radar by −0.11 m/s with a precision of 0.11 m/s, while the bias and precision in the POLCOMS current direction are 0° and 23°. However, the errors have a strong spatial pattern. Current direction is biased low (by as much as −15°) against the HF radar east of 3.6°W and biased high (up to +15°) on the west part of the HF radar domain. This highlights that good performance of the model in one area does not guarantee good performance across the whole domain or at all times, thus urging caution about relying solely on output from ocean models to validate new sensors.

Comparisons between POLCOMS and the Wavemill retrieved current averaged over all runs confirm the strong overall bias in POLCOMS current magnitude of −0.22 m/s against Wavemill data at the time of maximum ebb, and the slightly better correspondence in the western part of the domain. Although the Wavemill data could not enable the same detailed analyses as achievable with time series of HF radar data, this indicates that Wavemill's synoptic maps of ocean current vectors would be highly valuable in the absence of HF radar data to characterise the magnitude and spatial distribution of biases in predicted model currents.

4.4. A case study: effects of underwater bathymetry

This section takes a closer look at runs R3 and R4, which were acquired over the same ground track about 10 min apart with different flight and look directions, thereby providing a vicarious way of checking the quality of the retrieved currents. The main interest however lies in the deep bathymetry channel that is sampled by both tracks close to the mouth of the River Dee estuary, and which gives the means of examining the effect of sharply varying bathymetry on the Wavemill data.

Fig. 4-f indicates that R3 and R4 show generally good agreement in the ocean current field depicted, with both runs showing similar current magnitude and a strong coastal jet in the southernmost part of each run. Good agreement between the retrieved current in R3 and R4 is pleasing here since the data were acquired with radically different viewing directions with respect to the wind and no inter-run bias correction was applied to R3 (due to the lack of retrieved current for R3 at MBL needed for the inter-run bias correction).

Figs. 6 and 7 focus more closely on the southern part of the R3 and R4 runs, south of 53.40°N. Fig. 6 presents the retrieved surface current magnitude and direction for (left) R3, (middle) R4 and (right) the high-resolution bathymetry at 180 m spatial resolution. In these figures, the spatial resolution of the Wavemill data is 100 m.

Fig. 6 shows the very strong coastal jet that reaches up to 1.5 m/s in both runs. This jet is co-located with a deep water channel seen in the high-resolution bathymetry data, where water depth rapidly increases beyond 10 m in an otherwise relatively shallow area (depth less than 5 m). Unfortunately, no HF radar or POLCOMS current data are available for this deeper bathymetry channel because of the very coastal location of this feature.

There is good agreement also in the retrieved current direction between the two runs in the area of strong current, but with larger discrepancies in direction further offshore in R3, possibly due to the lack of inter-run bias correction in R3.

The bathymetry feature is clearly seen in the Wavemill amplitude data and retrieved current profiles shown in Fig. 7, where both amplitude and retrieved current speed increase over sharp water depth gradients. The impact on Wavemill amplitude is more clearly visible in data obtained from the R3 and R4 aft-looking antennas, which are looking close to the downwind and upwind directions respectively.

Fig. 7 (middle) highlights the very good agreement between the retrieved current speed profiles obtained in R3 and R4. There is a constant bias of about 0.18 m/s between the two profiles, once again

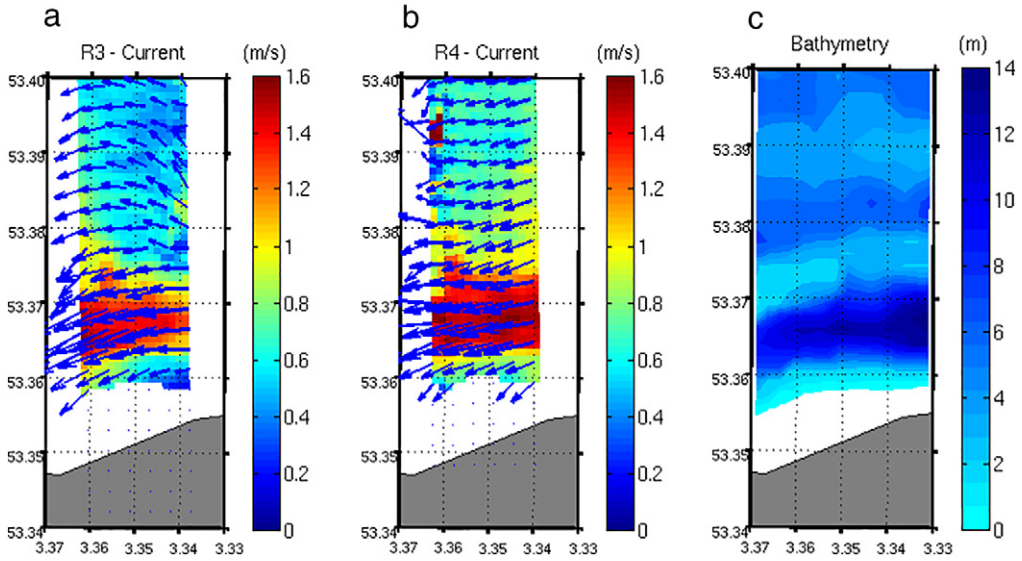

Fig. 6. (a) and (b) Zoomed-up view of the Wavemill retrieved surface currents in the southern part of (a) R3 and (b) R4. Colors represent the Wavemill current magnitude at 100m resolution. Arrows represent the Wavemill current direction subsampled to 300m to improve readability. Values over land have been discarded. (c) Bathymetry at 180m resolution over the area shown in (a) and (b).

likely due to the lack of inter-run calibration of R3. The retrieved current profiles broadly mirror the bathymetry profile, but with a slight position offset northwards.

Evidence of bathymetry effects is found also in other Wavemill runs, most notably in the southern part of R2, where an anomalously strong retrieved current (greater than 1 m/s around 53.37°N, 3.66°W) is associated with a rapid change in bathymetry, albeit in slightly deeper average water depth (∼ 10 m) than for R3 and R4. The HF radar also detects a slight increase in current magnitude in this area (Fig. 5a), but the current signature is less intense than in Wavemill data, probably because of the coarser 4 km spatial resolution of the HF radar.

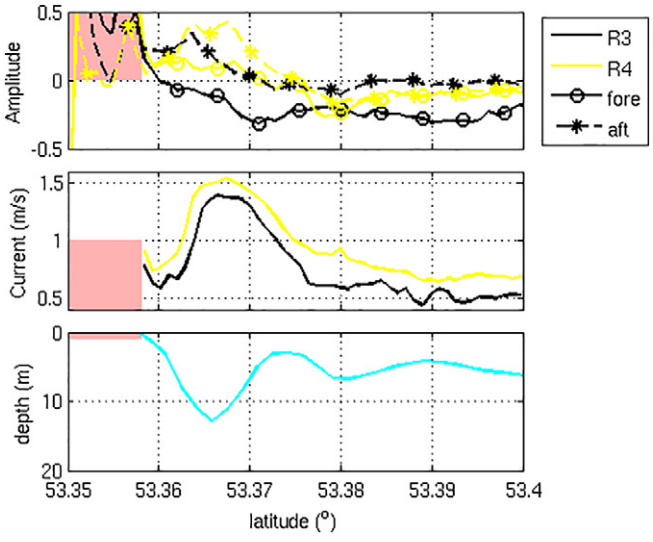

Fig. 7. Wavemill latitude profiles in the southern part of R3 and R4 shown in Fig. 6. Profiles are the median values calculated across-track of (top) SAR normalized amplitude and (middle) Wavemill retrieved surface current as a function of latitude. R3 is represented in black, R4 in yellow. The along-track resolution is 100 m. (bottom) Bathymetry over the same track as a function of latitude. The pink color background indicates land where Wavemill data are invalid.

5. Discussion

Validation of the Wavemill airborne retrieved surface currents against HF radar surface current estimates gives very encouraging results. Assuming uniform and constant wind conditions (5.5 m/s from 200°) over the whole area and using HF radar currents averaged over the 80 min flight duration, Wavemill reports biases and precisions typically better than 0.05 m/s and 0.1 m/s for surface current speed, and better than 10° and 7° for current direction, after correcting for intra-run biases at the cross-over over the MBL area.

Interestingly, the agreement between Wavemill and ADCP data at the Mersey Bar Light (MBL) buoy is even more striking than with the HF radar: at MBL, Wavemill current vectors match ADCP measurements within 0.02 m/s and 1° in magnitude and direction, which is better than the ≈10° bias observed for Wavemill current direction against the HF radar. However, the HF radar current direction is itself biased by about 10° against the ADCP data at MBL, and this could indicate a sensitivity of HF radar currents to other ocean surface effects (e.g. ocean surface waves) that are not present in ADCP and Wavemill data. Like for all Earth Observation measurements, validation against other types of surface current data is non-trivial. Even between HF radar and ADCP, there is no consensus about the impact of the Stokes drift on the measurements (see e.g. Ardhuin et al., 2009; Röhrs et al., 2015). Here, the airborne data are simply compared against HF radar and ADCP without presuming if differences are due to the differences in current depth sensitivity or to other reasons. Unfortunately, the data available in this campaign are insufficient to explore this further. Extensive in situ and airborne campaigns would be needed to estimate precisely the geophysical sensitivity of these different observations.

In the MBL area, where the runs have been inter-calibrated to provide spatially consistent current vector fields, the inter-run biases are of the order of ±0.1 m/s. These biases originate from minor differences between the WASV estimated from Wavemill (Martin et al., 2016) and the C-DOP model (Mouche et al., 2012), although these differences fall within the error bars of the C-DOP model. The origins of these small differences are not clear but could be due partly to the peculiar geophysical conditions of this campaign (short fetch; shallow bathymetry; wind, swell, current in opposing directions). These issues were discussed extensively in Martin et al. (2016).

Changing the wind speed used as input to the WASV correction by up to ± 1 m/s makes little difference to the Wavemill current retrieval performance, but changing the wind direction by ±15° significantly degrades the accuracy of the airborne current speed against the HF radar by about ± 0.2 m/s.

If one validates against the best temporally co-located HF radar current (available every 20 min), the Wavemill current retrieval statistics remain the same, except for R2 for which the bias improves from 0.06 m/s to 0.00 m/s.

For individual runs, the precision (standard deviation) of the retrieved surface currents is better than 0.1 m/s in magnitude and 7° in direction, except for R2, R5 and R8. For the bias, values are typically better than 0.06 m/s in magnitude and 11° in direction except for R8. Possible reasons for the poorer performance for these runs are examined next.

The poor precision of R2 against HF radar estimates (0.19 m/s) could be explained partly by small scale current variability associated with bathymetry that is resolved by the Wavemill system and not by the HF radar. In Section 4.4, a strong current of 1 m/s detected in R2 was found to be co-located with a bathymetry feature. The HF radar reported much weaker current intensification over the same feature, possibly due to its coarser 4×4 km spatial averaging. Moreover, the R2 track is closely aligned with the line-of-sight between the two HF radar antennas, raising questions about the reliability of the HF radar current estimates in these locations (as suggested by the large current speed ranges of up to 0.4 m/s seen in Fig. 2b).

R5 gives the second poorest precision against HF radar estimates (0.14 m/s). This can be traced to two large current speed anomalies against the HF radar data at the two extreme ends of the run. There are no apparent reasons for these anomalies other than they also correspond to HF radar cells at the edge of the HF radar domain where errors in the HF radar data could be larger. When excluding these two extreme points, the precision of Wavemill in R5 improves significantly (to 0.08 m/s).

R8 is dominated by a strong bias of 0.13 m/s that strongly impacts its RMSE. As part of the wind sensitivity analysis in Section 4.2, we find that the R8 bias against HF radar decreases when the WASV correction is computed with a wind direction of 185° instead of 200° (i.e. −15° from the assumed nominal wind direction). As R8 occurred about one hour after R2, it is possible that the wind direction changed slightly during the flight period. A small anti-clockwise rotation of the wind vector during that period is supported by the forecasts from the MetOffice UKV model (Figs. 2f and 3d), although not by the in situ measurements at Hilbre Island (Fig. 3f). However, with Hilbre Island situated at the mouth of the Dee River estuary, it may not give a sufficiently reliable representation of changes in wind direction further offshore in Liverpool Bay. In the absence of better wind information and no amplitude calibration of the Wavemill airborne system, it is impossible to be conclusive about a possible wind direction change being responsible for the slightly increased bias in R8.

Analyses of Wavemill currents against output from the POLCOMS model confirm the value of Wavemill's synoptic maps of current vectors for the validation and development of high-resolution ocean circulation models. When considering data over several tidal cycles, POLCOMS currents show very good agreement with the HF radar (correlation of 0.9 of spatial fields over two tidal cycles) but the model displays a systematic lag of about 1 h in the timing of the maximal ebb flow in the MBL area. Comparison of POLCOMS against HF radar data for the 80 min of the Wavemill flight during maximum ebbing flow indicates a negative bias of 0.19 m/s against HF radar currents, that varies across the domain. Comparisons of POLCOMS against Wavemill data leads to similar results. The airborne campaign confirms the ability of Wavemill to deliver high-accuracy maps of current vectors that can help to characterise the magnitude and spatial distribution of current errors in high-resolution models and support the validation and development of improved models and parameterizations.

Comparisons of runs R3 and R4 — acquired over the same ground-track but with radically different viewing directions with respect to the wind — provide further confirmation of the quality of the Wavemill currents. Surface currents retrieved for the two runs are in very good agreement, with both detecting a strong narrow coastal jet in the southernmost part of the track that is collocated with a small deeper water channel located close to the coast where no HF radar or POLCOMS data are available. The analyses also provide added confidence in the Wavemill retrieval method, with good results obtained with the straight-forward wind-dependent WASV correction without special adjustments for effects linked to fetch, sea wave development or wave-current interactions over shallow bathymetry. This suggests that these effects may be of secondary importance, at least according to the evidence from this airborne campaign. This hypothesis would need to be confirmed with further dedicated campaigns to confirm the performance of Wavemill in different fetch, sea state and current gradients conditions. The study confirms Wavemill's ability to detect strong localized ocean current jets associated with even relatively modest changes in bathymetry. The ability to retrieve surface current vectors remotely and accurately at a spatial resolution of 100 m in very coastal shallow waters is very encouraging and confirms the additional usefulness of a future Wavemill satellite mission for coastal applications and modeling.

6. Conclusions

The surface current vectors maps from the Wavemill airborne demonstrator examined in this paper represent the first example data ever obtained with a squinted along-track interferometric system that is compatible with implementation as a future satellite mission. Validation against measurements from HF radar and ADCP confirms the very good performance of the Wavemill concept for high-resolution mapping and accurate determination of ocean surface current vectors from single-pass measurements. The current field mapping and retrieval performance of Wavemill estimated against HF radar data - with bias and precision typically better than 0.05 m/s and 0.1 m/s for surface current speed, and better than 10°and7° for direction — provide evidence about the relevance of this new remote sensing observing capability for ocean surface current vectors.

The agreement between Wavemill and ADCP data at the Mersey Bar Light (MBL) buoy is even better, with errors within 0.02 m/s and 1° in magnitude and direction (compared to errors of the order of 10° for the retrieved current direction against HF radar). This small difference raises again the interesting wider question about the nature of the surface current that is sensed by different remote sensing and in situ instruments (see e.g. Ardhuin et al., 2009; Röhrs et al., 2015), and about the best choice of independent data to validate measurements from new remote sensors such as Wavemill.

Comparisons with output from the POLCOMS high-resolution ocean model were less compelling. Although the model gives very good agreement with the HF radar measurements when averaging over 48 h, the lack of spatial variability in the model surface current field and its 0.2 m/s underestimation of the surface current speed at the maximum ebbing flow leads to poor results against the HF radar and Wavemill at the time of the flights (correlation of instantaneous spatial fields < 0.5). This reminds us that model output should be used with caution when attempting to assess the validity of measurements from new sensors, particularly at high spatial resolution and in complex oceanographic environments such as was the case here. The work highlights the value for model validation and development of Wavemill's synoptic maps of ocean current vectors to quantify and characterise the spatial distribution of surface

current errors, although it is recognized that a few Wavemill overpasses cannot support the same degree of detailed analyses that can be achieved with time series of HF radar current maps.

The very good results obtained against HF radar and ADCP also give increased confidence in the validity of the Wavemill processing and the surface current retrieval methodology presented in this paper. Removing the Wind-wave induced Artefact Surface Velocity (WASV) in each azimuth look direction before calculating the current vector proves to be an essential step to successfully retrieve surface currents with squinted ATI SAR. Estimating the WASV could a priori have been challenging because of the strongly atypical geophysical conditions encountered during the campaign. The westward 0.7 m/s current, light southerly offshore wind and north-west swell produced a complex set of crossing wind/waves/currents that led to a mixed sea of fetch limited wind waves and low-amplitude crossing swell waves travelling across a strong tidal current over relatively shallow bathymetry. Still, despite these complex surface roughness conditions, the Mouche et al. (2012) empirical model was nevertheless suitable to independently estimate and remove the artefact velocity contribution by wind waves, and this, without adjustment for swell, wind/wave/current interactions or fetch-limited conditions. This suggests that these effects are of secondary importance for the WASV, at least for the data obtained in this campaign.

The retrieval performance reported in this paper was achieved under the forced assumption of uniform and constant wind conditions over the whole area and the full 80 min of the flights. This assumption, imposed by the lack of system amplitude calibration and of reliable ancillary wind data away from the coast, could be responsible for the slightly poorer results observed in some runs and look directions. The quality of the current retrieval was shown to be strongly sensitive to the choice of wind used to compute the WASV, particularly direction, so the spatial variation in surface wind one would naturally expect over an area such as this one could lead to local anomalies in the retrieved current that will degrade overall performance. This sensitivity to wind knowledge is the basis for the recommendation that future systems must provide calibrated amplitude data to make it possible for wind vector and current vector to be estimated simultaneously in every cell from the Wavemill data alone.

Conversely, the observed poorer retrievals in some runs and look directions could be related to secondary sea surface effects linked to swell, wind/wave/current interactions or fetch that are concealed by the constant uniform wind assumption. Some minor differences were pointed out by Martin et al. (2016) between the WASV estimated from the Wavemill data at MBL and Mouche et al. (2012) and could explain the small inter-run biases as well as the slightly larger errors obtained in some runs and look directions. Once again, the lack of offshore wind information and limited amount of data prevents more in-depth analyses but this is worthy of investigation in future airborne campaigns obtained in different settings and environmental conditions.

Finally, the Wavemill airborne data provides exciting new evidence about the ability of the instrument to detect and estimate strong current jets associated with deeper underwater bathymetry channels. Several high current anomalies detected in Wavemill data turn out to be linked to rapid changes in water depths in shallow waters (< 10 m). This introduces Wavemill as a new remote sensing capability to retrieve currents with 100 m spatial resolution even in shallow waters and close to the coast, where HF radar and models do not typically operate, and which should be of interest to coastal management and monitoring applications and shallow water modeling. Moreover, the bathymetry-related current anomalies contribute in part to the dispersion of the Wavemill measurements against the 4 km resolution HF radar measurements, which do not resolve these small intense features, so that the actual precision of Wavemill for current vector retrieval will in fact be better than the figures reported above.

Acknowledgments

The authors would like to thank Sam Doody, José Marquez (Airbus Defence & Space Ltd, UK) and Victor Navarro (Starlab Ltd, UK) for acquiring and processing the data from the Wavemill airborne campaign and for providing the Wavemill amplitude images and interferograms. The Wavemill airborne demonstrator data were acquired by Airbus Defence & Space UK under contract for the European Space Agency. The authors also gratefully acknowledge the support from John Howarth and Lucy Bricheno (National Oceanography Centre, Liverpool, UK) for providing the in situ data in Liverpool Bay (ADCP, HF radar, Hilbre wind station, bathymetry) and access to model output (POLCOMS, MetOffice atmospheric model) over Liverpool Bay and the Irish Sea. We are grateful to Alexis Mouche (Ifremer, France) for providing the C-DOP model. This research was supported by National Capability funding at the National Oceanography Centre from the Natural Environment Research Council (NERC), UK.

References

Ardhuin, F., Marié, L., Rascle, N., Forget, P., Roland, A., 2009. Observation and estimation of Lagrangian, Stokes, and Eulerian currents induced by wind and waves at the sea surface. J. Phys. Oceanogr. 39, 2820–2838. http://dx.doi.org/10.1175/2009JPO4169.1.

Bentamy, A., Grodsky, S.A., Elyouncha, A., Chapron, B., Desbiolles, F., 2016. Homogenization of scatterometer wind retrievals. Int. J. Climatol. http://dx.doi.org/10.1002/joc.4746.

Buck, C., 2005. An extension to the wide swath ocean altimeter concept. Geoscience and Remote Sensing Symposium, 2005. IGARSS '05. Proceedings. 2005 IEEE International. vol. 8. pp. 5436–5439. http://dx.doi.org/10.1109/IGARSS.2005.1525970.

Chapron, B., Collard, F., Ardhuin, F., 2005. Direct measurements of ocean surface velocity from space: interpretation and validation. J. Geophys. Res. Oceans 110, http://dx.doi.org/10.1029/2004JC002809.

Dibarboure, G., Boy, F., Desjonqueres, J.D., Labroue, S., Lasne, Y., Picot, N., Poisson, J.C., Thibaut, P., 2014. Investigating short-wavelength correlated errors on low-resolution mode altimetry. J. Atmos. Ocean. Technol. 31, 1337–1362. http://dx.doi.org/10.1175/JTECH-D-13-00081.1.

Emery, W.J., Thomas, A.C., Collins, M.J., Crawford, W.R., Mackas, D.L., 1986. An objective method for computing advective surface velocities from sequential infrared satellite images. J. Geophys. Res. Oceans 91, http://dx.doi.org/10.1029/JC091iC11p12865.

Farquharson, G., Aslebagh, S., Romeiser, R., 2016. Estimating nearshore ocean currents from airborne ati-sar. Proceedings of EUSAR 2016: 11th European Conference on Synthetic Aperture Radar. pp. 1–5.

Farquharson, G., Deng, H., Goncharenko, Y., Mower, J., 2014a. Dual-beam ati sar measurements of surface currents in the nearshore ocean. 2014 IEEE Geoscience and Remote Sensing Symposium. pp. 2661–2664. http://dx.doi.org/10.1109/IGARSS.2014.6947021.

Farquharson, G., Deng, H., Goncharenko, Y., Mower, J., 2014b. Measurements of the nearshore ocean with fmcw ati sar. EUSAR 2014; 10th European Conference on Synthetic Aperture Radar. pp. 1–4.

Farquharson, G., Junek, W., Ramanathan, A., Frasier, S., Tessier, R., McLaughlin, D., Sletten, M., Toporkov, J., 2004. A pod-based dual-beam SAR. IEEE Geosci. Remote Sens. Lett. 1, 62–65. http://dx.doi.org/10.1109/LGRS.2004.826553.

Frasier, S., Camps, A., 2001. Dual-beam interferometry for ocean surface current vector mapping. IEEE Trans. Geosci. Remote Sens. 39, 401–414. http://dx.doi.org/10.1109/36.905248.

Fu, L.-L., Chelton, D.B., Le Traon, P.-Y., Morrow, R., 2010. Eddy dynamics from satellite altimetry. Oceanography 14–25. http://dx.doi.org/10.5670/oceanog.2010.02.

Goldstein, R., Zebker, H., 1987. Interferometric radar measurement of ocean surface currents. Nature 328, 707–709.

Goldstein, R.M., Barnett, T.P., Zebker, H.A., 1989. Remote sensing of ocean currents. Science 246, 1282–1285. http://www.jstor.org/stable/1704623.

Graber, H.C., Thompson, D.R., Carande, R.E., 1996. Ocean surface features and currents measured with synthetic aperture radar interferometry and HF radar. J. Geophys. Res. Oceans 101, 25813–25832. http://dx.doi.org/10.1029/96JC02241.

Holt, J.T., James, I.D., 2001. An s-coordinate density evolving model of the north west european continental shelf. part 1 model description and density structure. J. Geophys. Res. 106, 14015–14034.

Kelly, K.A., 1989. An inverse model for near-surface velocity from infrared images. J. Phys. Oceanogr. 19, 1845–1864. http://dx.doi.org/10.1175/1520-0485(1989)019¡1845:AIMFNS¿2.0.CO;2.

Lane, A., 2008. A 3-d numerical model of liverpool bay for the coastal observatory. PECS 2008: Physics of Estuaries and Coastal Seas, Liverpool, UK, 25th–29th August 2008. pp. 415–418. http://nora.nerc.ac.uk/id/eprint/6487.

Lapeyre, G., Klein, P., 2006a. Dynamics of the upper oceanic layers in terms of surface quasigeostrophy theory. J. Phys. Oceanogr. 36, 165–176. http://dx.doi.org/10.1175/JPO2840.1.

Lapeyre, G., Klein, P., 2006b. Impact of the small-scale elongated filaments on the oceanic vertical pump. J. Mar. Res. 64, 835–851. http://www.ingentaconnect.com/content/jmr/jmr/2006/00000064/00000006/art00004. http://dx.doi.org/10.1357/002224006779698369.

Lévy, M., Klein, P., Tréguier, A.M., Iovino, D., Madec, G., Masson, S., Takahashi, K., 2010. Modifications of gyre circulation by sub-mesoscale physics. Ocean Model. 34, 1–15. http://www.sciencedirect.com/science/article/pii/S1463500310000582. http://dx.doi.org/10.1016/j.ocemod.2010.04.001.

Liu, Y., Weisberg, R.H., Merz, C.R., 2014. Assessment of CODAR SeaSonde and WERA HF radars in mapping surface currents on the west Florida shelf. J. Atmos. Ocean. Technol. 31, 1363–1382. http://dx.doi.org/10.1175/JTECH-D-13-00107.1.

Lyzenga, D.R., Shuchman, R.A., Rufenach, C.L., 1982. Synthetic aperture radar measurements of ocean surface currents. Geophys. Res. Lett. 9, 747–750. http://dx.doi.org/10.1029/GL009i007p00747.

Martin, A.C.H., Gommenginger, C., Marquez, J., Doody, S., Navarro, V., Buck, C., 2016. Wind-wave induced velocity in ATI SAR ocean surface currents: first experimental evidence from an airborne campaign. J. Geophys. Res. Oceans http://dx.doi.org/10.1002/2015JC011459.

Martin, A.P., Richards, K.J., 2001. Mechanisms for vertical nutrient transport within a north Atlantic mesoscale eddy. Deep-Sea Res. II Top. Stud. Oceanogr. 48, 757–773. http://www.sciencedirect.com/science/article/pii/S0967064500000965. http://dx.doi.org/10.1016/S0967-0645(00)00096-5.

Mouche, A., Collard, F., Chapron, B., Dagestad, K., Guitton, G., Johannessen, J., Kerbaol, V., Hansen, M., 2012. On the use of Doppler shift for sea surface wind retrieval from SAR. IEEE Trans. Geosci. Remote Sens. 50, http://dx.doi.org/10.1109/TGRS.2011.2174998.

Poje, A.C., Özgökmen, T.M., Lipphardt, B.L., Haus, B.K., Ryan, E.H., Haza, A.C., Jacobs, G.A., Reniers, A.J.H.M., Olascoaga, M.J., Novelli, G., Griffa, A., Beron-Vera, F.J., Chen, S.S., Coelho, E., Hogan, P.J., Kirwan, A.D., Huntley, H.S., Mariano, A.J., 2014. Submesoscale dispersion in the vicinity of the deepwater horizon spill. Proc. Natl. Acad. Sci. 111, 12693–12698. http://www.pnas.org/content/111/35/12693.abstract. http://dx.doi.org/10.1073/pnas.1402452111.

Röhrs, J., Sperrevik, A., Christensen, K., Broström, G., Breivik, Ø., 2015. Comparison of HF radar measurements with Eulerian and Lagrangian surface currents. Ocean Dyn. 65, 679–690. http://dx.doi.org/10.1007/s10236-015-0828-8.

Romeiser, R., Runge, H., Suchandt, S., Kahle, R., Rossi, C., Bell, P., 2014. Quality assessment of surface current fields from TerraSAR-X and TanDEM-X along-track interferometry and Doppler centroid analysis. IEEE Trans. Geosci. Remote Sens. 52, 2759–2772. http://dx.doi.org/10.1109/TGRS.2013.2265659.

Rufenach, C.L., Shuchman, R.A., Lyzenga, D.R., 1983. Interpretation of synthetic aperture radar measurements of ocean currents. J. Geophys. Res. Oceans 88, 1867–1876. http://dx.doi.org/10.1029/JC088iC03p01867.

Sasaki, H., Klein, P., Qiu, B., Sasai, Y., 2014. Impact of oceanic-scale interactions on the seasonal modulation of ocean dynamics by the atmosphere. Nat. Commun. 5, http://dx.doi.org/10.1038/ncomms6636.

Shemer, L., Marom, M., Markman, D., 1993. Estimates of currents in the nearshore ocean region using interferometric synthetic aperture radar. J. Geophys. Res. Oceans 98, 7001–7010. http://dx.doi.org/10.1029/92JC02962.

Shuchman, R.A., Meadows, G.A., 1980. Airborne synthetic aperture radar observation of surf zone conditions. Geophys. Res. Lett. 7, 857–860. http://dx.doi.org/10.1029/GL007i011p00857.

Toporkov, J., Perkovic, D., Farquharson, G., Sletten, M., Frasier, S., 2005. Sea surface velocity vector retrieval using dual-beam interferometry: first demonstration. IEEE Trans. Geosci. Remote Sens. 43, 2494–2502. http://dx.doi.org/10.1109/TGRS.2005.848603.

Waller, J.A., Dance, S.L., Lawless, A.S., Nichols, N.K., Eyre, J.R., 2014. Representativity error for temperature and humidity using the met office high-resolution model. Q. J. R. Meteorol. Soc. 140, 1189–1197. http://dx.doi.org/10.1002/qj.2207.

Team, Wavemill PoC, 2012. Wavemill Proof-of-Concept Final Report: A Proof-of–concept Airborne Campaign using an Existing X-band Interferometric SAR Instrument. ref: WM-RP-ASU-SY-003 v1 ESA/ESTEC Contract No. 4000103580/11/NL/CT.